

# Improved Model and Analysis for RIS-Assisted Indoor Terahertz Wireless Networks

Zhi Chai, Jiajie Xu, *Member, IEEE*, Mohamed-Slim Alouini, *Fellow, IEEE*, Justin P. Coon, *Senior Member, IEEE*

**Abstract**—In this paper, we propose a new model for indoor THz communication assisted by RIS. We conduct a realistic modeling of indoor obstacles and analyze their impact on performance. Order statistics are applied to calculate the cumulative distribution functions (CDFs) of distances from the transmitter to the selected RIS, i.e., the nearest RIS in the bounded indoor environment to the transmitter, and from the selected RIS to the receiver. We calculate the coverage probability (CP) as a function of the RIS number, obstacle density, room size, and the transmitter’s location. By comparing the numerical results obtained from the analytical expressions with Monte Carlo simulations, we verify the accuracy of our analysis. Through the numerical results, it is observed that room size and obstacle density affect the CP in a significant way. However, by optimizing the transmitter’s location and increasing the RIS number deployed in the room, the CP can be significantly improved (e.g., an increase of around 15% by optimizing the transmitter’s location, and an increase of around 30% by increasing the RIS number deployed in the room).

**Index Terms**—RIS, THz, Poisson point process, performance analysis, stochastic geometry, order statistics

## I. INTRODUCTION

### A. Motivation

WITH the depletion of the current commercial spectrum, the soaring demand from consumers, and the emerging techniques such as virtual reality (VR) [1]–[3] and autonomous driving [4]–[6], the global mobile traffic is estimated to increase by 55% each year, and reach 5016 exabytes, with the transmission rate growing up to 1Tbps at the end of 2030 [7], [8]. Hence, more attention is paid to the terahertz (THz) spectrum due to the substantial bandwidth, the ultra-fast transmission rate [9], [10], and the ultra-low latency [11], [12]. THz communication also has a wide range of applications such as wireless local area networks (WLAN), wireless data centers, and space communication networks [13]. However, a side effect of using the THz spectrum is that the signal will experience severe path loss and be hugely attenuated by scatterers, which leads to limited coverage. Reconfigurable intelligent surface (RIS) technology, as widely studied, is regarded as one of the most potential solutions to enhance THz communication’s coverage. RIS is defined as a synthesized surface that has many antenna elements with tunable devices (e.g., positive-intrinsic-negative diodes, varactors) mounted

on top to manipulate the phase of the impinging waves to realize a constructive superposition after reflection [14]. The reflected signal with an enhanced amplitude can improve the SNR to achieve broader coverage. Because of the severe path loss issue, the majority of THz applications focus on indoor environments, such as kiosk downloads [15] (communication range:  $\sim 1\text{m}$ ), WLAN [16] (communication range:  $\sim 10\text{m}$ ), and data center networks [17] (communication range:  $< 20\text{m}$ ). To achieve a high coverage probability (CP), high transmission speed, and low latency, multiple RISs can be deployed in the indoor environment to facilitate THz communications. In this paper, focusing on indoor THz communication, with the assistance of RIS, we analyze the CP variation with respect to the room size, obstacle density, RIS number, and the transmitter’s location. We also maximize CP by optimizing the transmitter’s location and the deployed RIS number.

### B. Related Work

In this subsection, we first give an overview of the CP analysis in THz communications and then introduce the state-of-the-art RIS-assisted network performance analysis.

1) *CP Analysis in THz Communications*: In [18], the outage probability is explicitly derived for a transmitter-relay-receiver system model, and beam misalignment is taken into consideration at THz frequencies. In [19], an unmanned aerial vehicle (UAV) is used as a decode-and-forward (DF) relay in the THz communication system. In the proposed system, the transmit power that minimizes the outage power is derived. Compared with the fixed power allocation scheme, the outage probability obtained through transmit power optimization is 20% lower. Both [18] and [19] focus on the link-level outage probability of a THz wireless communication system, which cannot capture the outage/coverage probability of the THz wireless communication network, and cannot provide insights into THz applications from a statistical perspective. In [20], a relay selection scheme is proposed in radio frequency (RF) and THz hybrid wireless communication networks. It can be concluded that the scheme would choose nodes supporting THz communication when the demand for transmission rate is high or the transmitter-receiver distance is short. Otherwise, it will choose nodes supporting RF communication. In [21], a CP analysis of the downlink is derived in an RF/THz hybrid wireless communication network in the presence of interference using stochastic geometry. In [22], a coverage performance analysis towards user-centric THz networks is carried out. It is concluded that static or dynamic clustering in user-centric networks has advantages over the conventional

Z. Chai, and J. P. Coon are with the Department of Engineering Science, University of Oxford, Parks Road, Oxford, OX1 3PJ, United Kingdom. (e-mail: zhi.chai@eng.ox.ac.uk, justin.coon@eng.ox.ac.uk).

J. Xu and M.-S. Alouini are with the Computer, Electrical and Mathematical Sciences and Engineering Division, King Abdullah University of Science and Technology, Thuwal, 23955, Kingdom of Saudi Arabia. (e-mail: jiajie.xu.1@kaust.edu.sa, slim.alouini@kaust.edu.sa).

single base station (BS) association policy. It is worth pointing out that [21] and [22] do not consider relays in the system, which may cause an overestimation of the system as the transmission distance is limited in THz communication systems. Meanwhile, active relays, for example, DF-based relays considered in [18]–[20] and [23]–[27], require higher energy consumption, and may not be an optimal candidate in THz communication systems.

2) *Stochastic Geometry-Based Analysis of the RIS-Assisted Wireless Communication Network*: As a passive relay, RIS is widely researched to improve communication performance. In [28], base stations (BSs) and RISs are assumed to follow two independent homogeneous Poisson point processes (HPPPs), respectively. It is also assumed that the density of the BS is lower than the density of the RIS, and there is no LOS path. The association policy proposed in [28] follows the shortest distance principle<sup>1</sup>. Through a comparison with conventional networks, it is concluded that the RIS-assisted network can achieve higher capacity and energy efficiency under the condition that the RIS density is higher than the BS density. It is shown in [28] that when the BS density is higher than the RIS density, it is unnecessary to deploy RIS devices. In [29], an application scenario with multiple users, BSs, and RISs in the presence of interference from BSs and RISs is considered, the BSs are assumed to follow an HPPP while the RIS is assumed to follow a binomial point process (BPP), and the Laplace Transform of the received signal power, approximated aggregate interference, CP, ergodic capacity, and the energy efficiency are derived based on the assumptions. The analytical results are validated by Monte-Carlo simulations. In [30], stochastic geometry is used to analyze the performance of a RIS-aided multi-cell non-orthogonal multiple access (NOMA) network. It is shown in [30] that the achievable data rate reaches an upper limit with the increase in the RIS size and the path loss intercept can be enhanced to improve the network performance without influencing the bandwidth. In [31], the authors propose to coat RIS on a subset of scatterers in the environment, and the light-of-sight (LOS) probability is taken into consideration. The authors model the locations of BSs and users following two independent HPPPs. The scatterers follow the line boolean model proposed in [32]. It is concluded that the deployment of RIS highly improves the coverage regions of the BSs, and it is shown that 6 RIS/km<sup>2</sup> is enough to maintain the ratio of blind spots over the total area below 10<sup>-5</sup> when the scatterer density is 300 scatterer/km<sup>2</sup>. In [33], the spatial correlation between transmitters and RISs is described by using the Gaussian point process (GPP), and the CP expressions under a fixed association strategy and a nearest association strategy are derived in closed form in the presence of limited interference. It is also shown that the system performance is independent of the density of transmitters with the nearest association strategy when the scenario is interference-limited.

3) *RIS-Assisted indoor THz wireless network CP Analysis*: In [34], a ray tracing simulation was conducted for the RIS-

assisted THz indoor system. The coverage probability variation with respect to the signal-to-noise ratio threshold was given for up to four RISs. Yet, the deployment strategy and the association policy were not considered. In [35], stochastic geometry was applied to an indoor THz wireless network, and the optimal RIS density that can maximize the coverage of users in THz wireless networks was obtained in the presence of interference. It is worth pointing out that the RISs were assumed to attach some of the obstacles in the indoor environment. Besides the THz spectrum, similar investigations have been conducted in the millimeter wave (mmWave) spectrum. [36] discussed small-cell densification and RIS deployment for coverage improvement. For the RIS solution, the deployment of RISs was assumed on the walls of a room with the locations following the 1-dimensional HPPP, but the blockage effect was not considered. [37] considered a humanity mobility model to calculate the outage probability in an indoor environment and the RIS locations (assumed to be on the wall) were optimized with respect to coverage. However, the blockage and the RIS amount showed in the simulation section was up to 2 (e.g., 1 and 2 humans as the blockages, and 1 and 2 RISs being deployed on the wall). Such results cannot provide insight when the network scales up. In addition, [37] assumes multi-hop existed between RISs<sup>2</sup>, which is unclear currently whether RIS is feasible for this functionality. Compare [36], [37] with [35], [36], [37] is more practical in terms of deployment because the RISs were assumed to be deployed on the walls of a room rather than on obstacles<sup>3</sup>. What's more, both [35] and [36] did not consider the boundary effect (See Appendix A for details) of an indoor environment when conducting the analysis.

### C. Contributions

In this paper, we investigate the THz wireless communication network coverage performance in an indoor environment with boundaries considered. The main contributions are given below:

- *We propose a new RIS-assisted indoor THz communication model.* We explicitly consider the effects of boundaries. In addition, a new blockage model considering the size and density of the obstacle is proposed, which can describe the indoor environment more realistically.
- *We analytically characterize the coverage probability for the RIS-assisted indoor THz communication network.* The communication link is classified as the direct link (transmitter-receiver) and the indirect link (transmitter-RIS-receiver). In the indirect link, the association policy is that the nearest RIS will be selected as the desired RIS to reflect the signal. The combined coverage performance of the direct and indirect link is analyzed with the room size, RIS number, obstacle density, and transmitter's location as variables.
- *We maximize the CP by optimizing the transmitter's location and the deployed RIS number.* Based on the analytical

<sup>2</sup>The signal can be reflected twice by the RISs before it reaches the receiver.

<sup>3</sup>The obstacles may have irregular shapes, which is hard for RIS to be deployed on.

<sup>1</sup>The shortest distance principle means the user will associate the nearest RIS in the indirect path.

results and simulations, it is shown that the room size and the obstacle density are two factors that dominate the CP. However, by optimizing the transmitter's location and increasing the RIS number, a significant improvement (15% to 30%) to the CP can be observed. These relationships will serve as guidance in the future RIS-assisted indoor THz wireless communication network deployment.

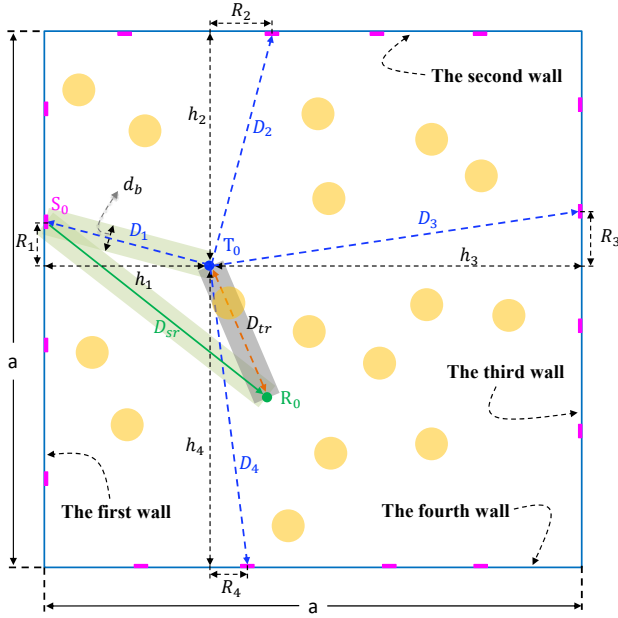


Fig. 1: RIS-assisted indoor THz wireless communication network illustration.

## II. SYSTEM MODEL

The RIS-assisted indoor THz wireless communication network is illustrated in Fig. 1. We consider a square-bounded region. The length and width of the square room are denoted as  $a$ . The deployment of RISs is restricted to the wall. It is assumed that each wall has the same number of RISs and the location of each RIS is an independent and identically distributed (i.i.d.) random variable following the uniform distribution  $\mathcal{U}(0, a)$ . The yellow circles with a constant diameter  $d_b$  in Fig. 1 represent obstacles. The transmitter's location is given, and receivers and the centers of obstacles are assumed to follow two independent HPPPs in the room. We define a transmitter as  $T_0$ , the nearest RIS to  $T_0$  as  $S_0$ , and a receiver as  $R_0$ . We apply a two-step communication strategy.  $T_0$  will first try to connect to  $R_0$  via the direct link, and the communication distance is denoted as  $D_{tr}$ .  $D_{tr}$  can be described as the distance between a given location (the transmitter) and a point subject to an HPPP. If the direct link is blocked, or the SNR is lower than the threshold,  $T_0$  will choose  $S_0$ , and then  $S_0$  will reflect the signal to the desired receiver on the condition that there are no obstacles between  $T_0$  and  $S_0$ , as well as  $S_0$  and  $R_0$ . For better tractability, as shown in Fig. 1, we define  $D_i$  to be the random variable that represents the shortest distance from  $T_0$  to the  $i$ th wall. Define  $R_i$  as the distance between the projection of  $T_0$  on the  $i$ th wall and the nearest RIS on that

wall.  $h_i$  is a constant describing the distance from  $T_0$  to the  $i$ th wall. We define  $D_{ts}$  as the minimum among  $D_i$ ,  $i = 1, 2, 3, 4$ , and  $D_{sr}$  as the distance between  $S_0$  and  $R_0$ . In addition, there are three highlighted rectangular areas between any two nodes in Fig. 1. These rectangular areas are related to the calculation of the LOS/NLOS probabilities and will be explained in detail later.

## III. DISTANCES DISTRIBUTIONS

### A. CDF expression of $D_{ts}$

According to the association policy,  $D_{ts}$  is the shortest distance between the transmitter and the RIS on the walls. We define  $\mathcal{D} = \{D_1, D_2, D_3, D_4\}$ ,  $\mathcal{R} = \{R_1, R_2, R_3, R_4\}$ , and  $\mathcal{H} = \{h_1, h_2, h_3, h_4\}$  as three sets. With the help of  $\mathcal{D}$  and  $\mathcal{R}$ ,  $D_{ts}$  can be expressed as

$$\begin{aligned} D_{ts} &= \min\{\mathcal{D}\} \\ &= \min\left\{\sqrt{\mathcal{R}^2 + \mathcal{H}^2}\right\}. \end{aligned} \quad (1)$$

From (1), it is noted that acquiring the CDF of  $R_i$  is necessary for calculating the CDF of  $D_{ts}$ . Because the RIS's location distribution is the same on every wall, we only show the derivation process of  $R_1$ . The CDF derivation processes of  $R_2$ ,  $R_3$ , and  $R_4$  are similar to  $R_1$ . Define the lower left corner of the room as the origin of the room. Define the location of the transmitter as  $(x_t, y_t)$ .  $X_1, X_2, \dots, X_n$  are  $n$  uniform random variables following  $\mathcal{U}(0, a)$  that represent the locations of the RISs on the first wall.  $Y_j$  represents the distance from the  $j$ th RIS to  $(0, y_t)$ . If  $y_t$  is smaller than  $a/2$ , the CDF of  $Y_j$  is given by

$$\begin{aligned} F_{Y_j}(y) &= P(Y_j \leq y) \\ &= P(|y_t - X_j| \leq y) \\ &= P(y_t - y \leq X_j \leq y_t + y) \\ &= \frac{1}{a} \left( \min\{a - y_t, y_t + y\} - \max\{0, y_t - y\} \right), \end{aligned} \quad (2)$$

if  $y_t$  is larger than  $a/2$ , the CDF of  $Y_i$  is given by

$$F_{Y_j}(y) = \frac{1}{a} \left( \min\{y_t, y_t + y\} - \max\{0, y_t - y\} \right). \quad (3)$$

Because  $X_1, X_2, \dots, X_n$  are i.i.d. uniform random variables,  $Y_1, Y_2, \dots, Y_n$  are also i.i.d. random variables with the CDF of (2) or (3).  $R_1$  can be interpreted as the first order variable among  $Y_1, Y_2, \dots, Y_n$ . Based on order statistics, the CDF of the first order variable is given by

$$F_{R_1}(r) = 1 - (1 - F_{Y_j}(r))^n. \quad (4)$$

Note that, when deriving the CDFs of  $R_2$ ,  $R_3$ , and  $R_4$ , the value of  $y_t$  should be replaced to the corresponding values (e.g.,  $x_t$  for  $R_2$ ,  $y_t$  for  $R_3$ , and  $x_t$  for  $R_4$ ). With the CDF of  $R_1$ , the CDF of  $D_1$  is given by

$$\begin{aligned}
F_{D_1}(d) &= P(D_1 \leq d) \\
&= P(\sqrt{R_1^2 + h_1^2} \leq d) \\
&= P(R_1 \leq \sqrt{d^2 - h_1^2}) \\
&= F_{R_1}(\sqrt{d^2 - h_1^2})\mathbb{1}(d, h_1), \tag{5}
\end{aligned}$$

where  $\mathbb{1}(a, b)$  is the indicator function.  $\mathbb{1}(a, b)$  is equal to 1 when  $a \geq b$ ,  $\mathbb{1}(a, b)$  is equal to 0 when  $a < b$ . As the CDF derivation steps of  $D_2$ ,  $D_3$ , and  $D_4$  are similar to  $D_1$ , we do not show the derivation details here. The CDF of  $D_i$  is given by

$$F_{D_i}(d) = F_{R_i}(\sqrt{d^2 - h_i^2})\mathbb{1}(d, h_i). \tag{6}$$

With the CDF of  $D_i$ , the CDF of  $D_{ts}$  can be calculated as

$$\begin{aligned}
F_{D_{ts}}(d) &= P(D_{ts} \leq d) \\
&= P(\min\{\mathcal{D}\} \leq d) \\
&= 1 - P(\min\{\mathcal{D}\} \geq d) \\
&= 1 - \prod_{i=1}^4 (1 - F_{D_i}(d)). \tag{7}
\end{aligned}$$

A comparison between the analytical expression of the CDF of  $D_{ts}$  and the Monte Carlo simulations is given in Fig. 2. The dashed lines represent the CDF of  $D_{ts}$  obtained from the analytical expression, and the solid lines represent the CDF of  $D_{ts}$  obtained from the Monte Carlo simulations. It is noted that there is a high match between the dashed lines and solid lines, which indicates the accuracy of the derived analytical expression.

As we already obtain the CDF expression of  $D_{ts}$  related to the first communication step in the indirect link, we will forward to the second communication step and analyze the related CDF expression in the following.

### B. CDF Expression of $D_{sr}$

We first show the exact analytical expression of the CDF of  $D_{sr}$ . This is given by

$$\begin{aligned}
F_{D_{sr}}(d) &= \sum_{i=1}^4 F_{D_{sr}}(d | D_i = \min\{\mathcal{D}\}) \\
&\quad \times P(D_i = \min\{\mathcal{D}\}) \\
&= \sum_{i=1}^4 F_{D_{sr}}(d | D_i = \min\{\sqrt{\mathcal{R}^2 + \mathcal{H}^2}\}) \\
&\quad \times P(D_i = \min\{\mathcal{D}\}). \tag{8}
\end{aligned}$$

Then, we show how to calculate the fourth term in the summation in (8) (The calculation steps for other terms are similar to the fourth term). For now, we assume the selected RIS is on the fourth wall, and omit the probability term in the

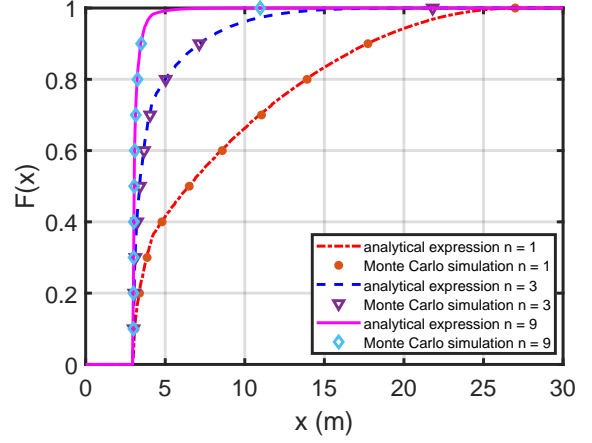


Fig. 2: CDF of  $D_{ts}$  comparison between the Monte Carlo simulations and the analytical expression with  $a = 30$  m,  $x_t = 3$  m,  $y_t = 27$  m and the RIS number on one wall  $n = 1, 3, 9$ .

fourth term. Define  $(X_r, Y_r)$  as the coordinate of the receiver. Because the receiver follows HPPP,  $X_r$  and  $Y_r$  are two i.i.d. random variables following uniform distribution  $\mathcal{U}(0, a)$ . By observing the geometry relationship between the transmitter, receiver, and selected RIS in Fig. 3, we find that  $D_{sr}$  can be represented by  $X_r, Y_r, x_t, y_t, h_4$  and  $R_4$ . The expression is given by

$$D_{sr} = \sqrt{(R_4 + (X_r - x_t))^2 + (h_4 + (Y_r - y_t))^2}, \tag{9}$$

and the expression of the fourth term (with the conditions omitted) is given by

$$\begin{aligned}
F_{D_{sr}}(d | D_4) &= P(D_{sr} \leq d) \\
&= P(\sqrt{(R_4 + (X_r - x_t))^2 + (h_4 + (Y_r - y_t))^2} \leq d) \\
&= P((R_4 + (X_r - x_t))^2 \leq d^2 - (h_4 + (Y_r - y_t))^2) \\
&\stackrel{(a)}{=} \underbrace{P(x_t - X_r \leq R_4 \leq x_t - X_r + \sqrt{d^2 - (h_4 + (Y_r - y_t))^2})}_{P_1} \\
&\quad + \underbrace{P(x_t - X_r - \sqrt{d^2 - (h_4 + (Y_r - y_t))^2} \leq R_4 \leq x_t - X_r)}_{P_2}, \tag{10}
\end{aligned}$$

where (a) in (10) comes from that the term  $R_4 + (X_r - x_t)$  can be negative or positive. The first term (defined as  $P_1$ ) in (10) can be expanded as (11) and the second term (defined as  $P_2$ ) in (10) can be expanded as (12) (shown on the next page). Under the assumption of the selected RIS being on the fourth wall, three integrals are needed to calculate the CDF of  $D_{sr}$ . When we incorporate the probability in the fourth term, there will be six integrals, including the integrals with respect to  $R_1, R_2$ , and  $R_3$ . This suggests the direct calculation of  $F_{D_{sr}}(d)$  is not possible. We know most of the computation in the expression of  $F_{D_{sr}}(d)$  comes from deciding which wall the selected RIS is on. To simplify this process, we can use  $h_1, h_2, h_3$ , and  $h_4$  to approximate which wall has the selected

$$P_1 = \int_0^a \frac{1}{a} \int_0^a \frac{1}{a} \int_{\max\{0, x_t - x_r\}}^{\min\left\{a, x_t - x_r + \sqrt{\max\{0, d^2 - (h_4 + (y_r - y_t))^2\}}\right\}} f_{R_4}(r) dr dx_r dy_r. \quad (11)$$

$$P_2 = \int_0^a \frac{1}{a} \int_0^a \frac{1}{a} \int_{\max\left\{0, x_t - x_r - \sqrt{\max\{0, d^2 - (h_4 + (y_r - y_t))^2\}}\right\}}^{\min\{a, x_t - x_r\}} f_{R_4}(r) dr dx_r dy_r. \quad (12)$$

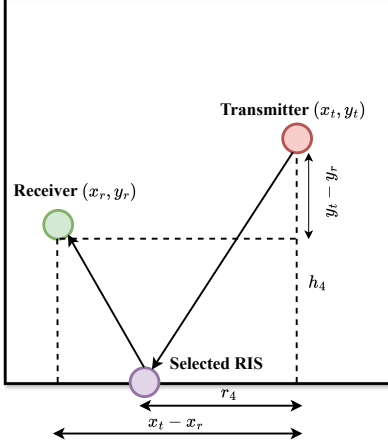


Fig. 3: Geometric illustration for CDF of  $D_{sr}$  calculation

RIS. For instance, if  $h_1$  is the minimum among  $h_1, h_2, h_3,$  and  $h_4$ , we assume the selected RIS is on the first wall<sup>4</sup>. We then show the comparisons between the approximated CDF of  $D_{sr}$  and the Monte Carlo simulations. In Fig. 4, the dots represent the Monte Carlo simulations, and solid lines represent the approximated analytical results. It is observed that there is a high match between the approximation and simulations. In the zoom-in figure, it is shown that the maximum deviation is around 0.05 at  $n = 3$ . We give more comparisons with different parameters in Appendix A to show the accuracy of the approximation. With the CDF of  $D_{ts}$  and  $D_{sr}$ , the analysis of the indirect link is completed. We then forward to the direct link where the CDF of  $D_{tr}$  will be described in the following.

### C. CDF Expression of $D_{tr}$

The location of the receiver can be defined as  $(X_r, Y_r)$ , with  $X_r$ , and  $Y_r$  follow  $\mathcal{U}(0, a)$ ,  $D_{tr}$  can be expressed as

$$D_{tr} = \sqrt{(X_r - x_t)^2 + (Y_r - y_t)^2}. \quad (13)$$

<sup>4</sup>The reason this method is not 100% accurate is that there may exist more than one minimum values. For instance,  $h_1 = h_2 < h_3 < h_4$ . Under this scenario, the selected RIS may show on the first wall or the second wall.

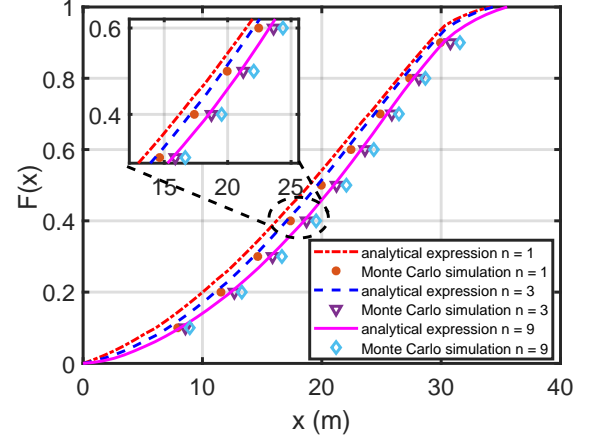


Fig. 4: CDF of  $D_{sr}$  comparison between the Monte Carlo simulation and the analytical expression with  $a = 30$  m,  $x_t = 3$  m,  $y_t = 27$  m, and the RIS number on a wall  $n = 1, 3, 9$ .

The CDF of  $D_{tr}$  is given by

$$\begin{aligned} F_{D_{tr}} &= P(D_{tr} \leq d) \\ &= P(\sqrt{(X_r - x_t)^2 + (Y_r - y_t)^2} \leq d) \\ &= P((X_r - x_t)^2 \leq d^2 - (Y_r - y_t)^2). \end{aligned} \quad (14)$$

Due to  $X_r - x_t$  can be positive or negative, (14) can be expanded as

$$\begin{aligned} &P((X_r - x_t)^2 \leq d^2 - (Y_r - y_t)^2) \\ &= P(x_t \leq X_r \leq x_t + \sqrt{d^2 - (Y_r - y_t)^2}) \\ &+ P(x_t - \sqrt{d^2 - (Y_r - y_t)^2} \leq X_r \leq x_t) \\ &= P(x_t \leq x_r \leq x_t + \sqrt{d^2 - (y_r - y_t)^2} | x_r, y_r) \\ &+ P(x_t - \sqrt{d^2 - (y_r - y_t)^2} \leq x_r \leq x_t | x_r, y_r) \\ &= \int_0^a \frac{1}{a} \int_{x_t}^{\max\left\{a, x_t + \sqrt{\max\{0, d^2 - (y_r - y_t)^2\}}\right\}} \frac{1}{a} dx_r dy_r \\ &+ \int_0^a \frac{1}{a} \int_{\max\left\{0, x_t - \sqrt{\max\{0, d^2 - (y_r - y_t)^2\}}\right\}}^a \frac{1}{a} dx_r dy_r. \end{aligned} \quad (15)$$

**Remark 1.** In [38], a similar CDF was derived, i.e., the distance between a fixed point and a point generated by an HPPP. Interested readers can refer to page-224 to page-225 [38] for more details.

#### D. CP Expression

Before we derive the expression of CP, we briefly discuss the calculation of LOS/NLOS probability. Previous work related to LOS/NLOS probability calculation includes [32]. In [32], the LOS/NLOS probability of urban cellular networks was analyzed using random shape theory, where the obstacles are modeled as rectangles with the length and width being random variables, and obstacles' centers following PPP. It is worth pointing out that due to the mathematical model of the obstacle, the CP calculation in [32] has a high computational complexity. In this paper, we aim to simplify the obstacle modeling process. Such a simplification can reduce the computation time when the network scales up. We define the obstacle as a circle with a diameter of  $d_b$ . If the communication link, which is assumed to be a line, is away from the obstacle's center more than the obstacle's radius, it will not be blocked. Otherwise, it will be blocked. The LOS probability then can be interpreted as the center of the obstacle not appearing in the corresponding rectangular area<sup>5</sup>. The NLOS probability can be interpreted as the center of the obstacle appearing in the corresponding rectangular area. To be clearer, one can refer to Fig. 1, where the rectangular area for any two nodes is highlighted. Then, the LOS probability for any two nodes  $P_{\text{LOS}}$ , whose expression can be given by

$$P_{\text{LOS-PQ}}^{\text{RV}} = e^{-\lambda_o D_{\text{PQ}} d_b}, \quad (16)$$

where  $D_{\text{PQ}}$ ,  $\text{PQ} = \{\text{TS}, \text{SR}, \text{TR}\}$  and  $\lambda_o$  represent the distance between two nodes and the obstacle density. As the distances between any two nodes are characterized as random variables in this context, the LOS probability in (16) is also a random variable. We use the expected value of (16) to describe the LOS probability, which is defined as

$$P_{\text{LOS-PQ}} = \mathbb{E}[e^{-\lambda_o D_{\text{PQ}} d_b}]. \quad (17)$$

The NLOS probability of any two nodes is given by

$$P_{\text{NLOS-PQ}} = 1 - \mathbb{E}[e^{-\lambda_o D_{\text{PQ}} d_b}]. \quad (18)$$

We then give the CP of the indirect link<sup>6</sup> and direct link<sup>7</sup> below:

$$\begin{aligned} P_{\text{cov}}^i &= P_{\text{LOS-TS}} P_{\text{LOS-SR}} P_{\text{NLOS-TR}} P(\text{SNR}_i \geq \tau) P(\text{SNR}_d \geq \tau) \\ &+ P_{\text{LOS-TS}} P_{\text{LOS-SR}} P_{\text{LOS-TR}} P(\text{SNR}_i \geq \tau) P(\text{SNR}_d \leq \tau) \\ &+ P_{\text{LOS-TS}} P_{\text{LOS-SR}} P_{\text{NLOS-TR}} P(\text{SNR}_i \geq \tau) P(\text{SNR}_d \leq \tau), \end{aligned} \quad (19)$$

$$P_{\text{cov}}^d = P_{\text{LOS-TR}} P(\text{SNR}_d \geq \tau), \quad (20)$$

<sup>5</sup>The rectangular area between any two nodes can be drawn by setting the node to be the middle point of the width, the obstacle diameter to be the width, and the transmission distance to be the length. For a clearer view, one can refer to Fig. 1, where the rectangular areas for any two nodes are highlighted.

<sup>6</sup>The link reflected from the RIS. When considering the indirect link, the direct link is assumed to be blocked, or the SNR of the direct link is lower than the threshold, or both.

<sup>7</sup>The link from the transmitter to the receiver, without the assistance of the RIS. When considering the direct link, there is no assumption of the indirect link.

Table I: Parameter settings for analytical expression validation.

Parameter	Value
$a$	[10, 20, 30, 40, 50, 60, 70, 80, 90, 100] m
$x_t$	$a/10$
$y_t$	$9a/10$
RIS amount on four walls	[20, 40, 60, 80, 100, 120, 140, 160, 180, 200]
$\lambda_o$	[0.01, 0.02, 0.05] points/m <sup>2</sup>
$M$	16
$d_b$	1 m
$P_{\text{Tx}}$	$1 \times 10^{-3}$ W
$\sigma^2$	$1 \times 10^{-12}$ W

where  $\text{SNR}_i$  and  $\text{SNR}_d$  denote the SNR for the indirect link and the SNR for the direct link. In the indirect link, we assume the RIS operates in the electrically small regime that the SNR is proportional to the square of the surface area and inversely proportional to the square of the multiplication of indirect distances [39]. Due to the beam being highly directive and narrow in the THz communication system and the angular selectivity [40] of the RIS, We assume that there is no interference from other RISs to an intended receiver. Hence, the term  $P(\text{SNR}_i \geq \tau)$  in (19) can be expressed as

$$\begin{aligned} P(\text{SNR}_i \geq \tau) &= P\left(\frac{P_{\text{Tx}} G_t G_r M^4}{\sigma^2} \left(\frac{\lambda}{4\pi D_{ts} D_{sr}}\right)^\alpha \geq \tau\right) \\ &= P\left(D_{sr} \leq \frac{\lambda}{4\pi D_{ts}} \left(\frac{P_{\text{Tx}} G_t G_r M^4}{\tau \sigma^2}\right)^{-\alpha}\right) \\ &= \int_0^a f_{D_{ts}}(d_{ts}) \int_0^{\frac{\lambda}{4\pi d_{ts}} \left(\frac{P_{\text{Tx}} G_t G_r M^4}{\tau \sigma^2}\right)^{-\alpha}} \\ &\quad \times f_{D_{sr}}(d_{sr}) dd_{sr} dd_{ts}, \end{aligned} \quad (21)$$

and the term  $P(\text{SNR}_d \geq \tau)$  can be expanded as

$$\begin{aligned} P(\text{SNR}_d \geq \tau) &= P\left(\frac{P_{\text{Tx}} G_t G_r}{\sigma^2} \left(\frac{\lambda}{4\pi D_{tr}}\right)^\alpha \geq \tau\right) \\ &= P\left(D_{tr} \leq \frac{\lambda}{4\pi} \left(\frac{P_{\text{Tx}} G_t G_r}{\tau \sigma^2}\right)^{\frac{1}{\alpha}}\right) \\ &= \int_0^{\frac{\lambda}{4\pi} \left(\frac{P_{\text{Tx}} G_t G_r}{\tau \sigma^2}\right)^{\frac{1}{\alpha}}} f_{D_{tr}}(d_{tr}) dd_{tr}, \end{aligned} \quad (22)$$

where  $P_{\text{Tx}}$ ,  $G_t$ ,  $G_r$ ,  $M$ ,  $\sigma^2$ ,  $\lambda$ ,  $\tau$ , and  $\alpha$  denote the transmitted power, the antenna gain of the transmitter, the antenna gain of the receiver, the RIS element number, noise power, the wavelength of the transmitted wave, the SNR threshold, and the attenuation factor.  $f_{D_{ts}}(d_{ts})$ ,  $f_{D_{sr}}(d_{sr})$ , and  $f_{D_{tr}}(d_{tr})$  are probability density functions (PDFs) of  $D_{ts}$ ,  $D_{sr}$ , and  $D_{tr}$  that can be obtained from the CDFs of  $D_{ts}$ ,  $D_{sr}$ , and  $D_{tr}$ , which have been given in the previous section. The total CP is calculated as

$$P_{\text{cov}} = P_{\text{cov}}^i + P_{\text{cov}}^d. \quad (23)$$

## IV. SIMULATIONS

### A. Analytical Expression Validation

We first give the parameter settings for the validation of the analytical expression in Table. I.

The comparison between the analytical results and the Monte Carlo simulations for a square room with the transmitter at the upper left corner of the room is shown in Fig. 5(a). Firstly, it is observed that there is a high match between the analytical curves and the Monte Carlo simulations for different obstacle densities. Secondly, it is noted that the CP will decrease with the increase in the room size. It can be noticed that compared with  $\lambda_o = 0.01$  and  $0.02$ , when  $\lambda = 0.05$ , the slope of the CP curve is more steep. This interesting phenomenon is expected as the result of the different LOS probabilities in direct and indirect links in different scenarios. To understand the trend of the three curves in Fig. 5(a) in a clearer way,  $P_{\text{LOS-TR}}$  and  $P_{\text{LOS-TS}}P_{\text{LOS-SR}}$  are shown in Fig. 5(b) and Fig. 5(c). As we can see, both  $P_{\text{LOS-TR}}$  and  $P_{\text{LOS-TS}}P_{\text{LOS-SR}}$  decrease fast along with the increase of the room size, which results in the steep slope of the curve for  $\lambda_o = 0.05$ . The relatively small slopes for  $\lambda_o = 0.01$  and  $0.02$  in Fig. 5(b) and Fig. 5(c) leads to the relatively gentle descent process on the CP. Fig. 5 indicates that the room size will have a more critical effect on the CP when the  $\lambda_o$  is bigger. To explore more insights, CP performance over different  $\lambda_o$  and room size is shown in Fig. 6. Observing Fig. 6 horizontally, CP decreases slowly over room size when  $\lambda_o$  is small, and fast when  $\lambda_o$  is large. Observing Fig. 6 vertically,  $\lambda_o$  dominates the CP performance when the room size is small. However, with the increase of the room size, the variation of  $\lambda_o$  has less and less effect on the CP performance.

### B. Investigation on the Transmitter Location

In the above subsection, we investigate the CP performance with the Tx placed at the upper left corner of the room. It is easy to understand that in the small size indoor environment for the THz wireless communication networks, the transmitter's location hugely affects the CP performance. In this subsection, we investigate four typical Tx locations as templates: (1) upper left corner of the room with the coordinate  $(x_t, y_t) = (a/10, 9a/10)$ , (2) center of the room with the coordinate  $(x_t, y_t) = (a/2, a/2)$ , (3) upper-middle of the room with the coordinate  $(x_t, y_t) = (a/2, 9a/10)$ , (4) middle point between location 1 and location 2 with the coordinate  $(x_t, y_t) = (3a/10, 7a/10)$ . We define these locations as the first, second, third, and fourth locations. We show the CP performance of the network in Fig. 7 for the last three different locations of the transmitter (the performance of the first location is shown in Fig. 5(a)). Comparing Fig. 5(a) with three sub-figures in Fig. 7, it is noted that the performance of Fig.7(b) is the best compared to others. This can be explained by examining the expected values of  $D_{ts}$  and  $D_{sr}$ . Because the third location is closer to the wall than the second and fourth locations (same compared to the first location), the expected value of  $D_{ts}$  of the third location is smaller than the second and fourth locations and equal to the first location. In addition, the expected value of  $D_{sr}$  of the third location

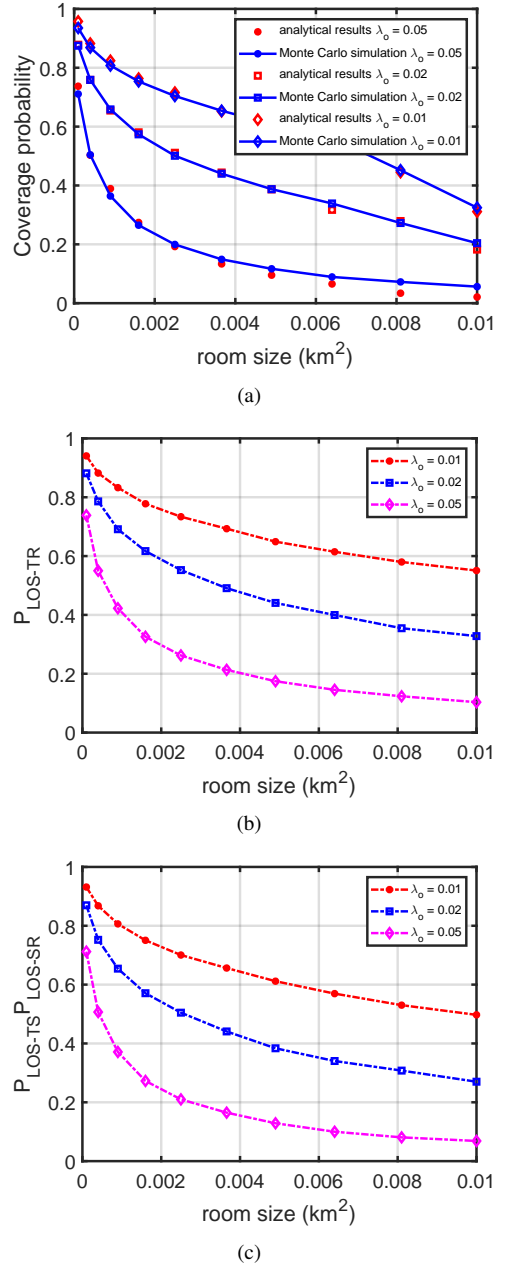


Fig. 5: (a) Performance comparison between the analytical results and the Monte Carlo simulations in a room with the transmitter being in the center of the room. (b) Simulated direct link LOS probability. (c) Simulated indirect link probability.

is smaller than the first and fourth locations<sup>8</sup>. Hence, Fig. 7(b) performs best. It is also noted that the performance in Fig. 7(a) is the worst. This is because the expected value of  $D_{ts}$  in Fig. 7(a) is larger than others, which leads to a worse CP performance. However, with the increase of the obstacle density, the performance improvement introduced by the transmitter location will diminish. To view the relationship

<sup>8</sup>The expected value of  $D_{sr}$  of the third location is larger than the second location. However, due to a large expected value of  $D_{ts}$ , the performance of the second is worse than the third location.

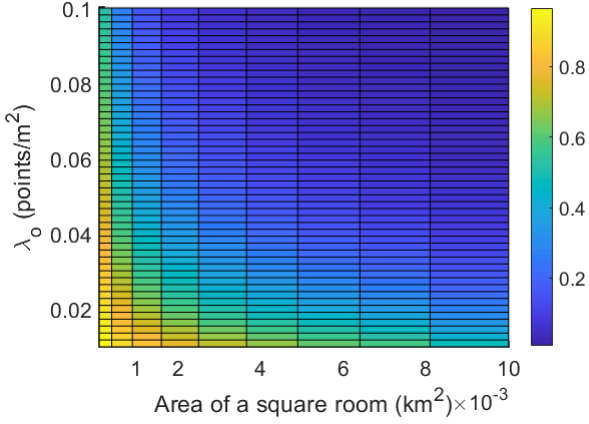


Fig. 6: Performance evaluation with respect to the room size and the obstacle density with the RIS amount, transmitted power, and transmitter location outlined in Table I.

between the transmitter's location and the performance of the network in a clearer way, we also provide a three-dimensional diagram. In Fig. 8, the horizontal axis represents the location of the transmitter on the  $x$ -axis, and the vertical axis represents the location of the transmitter on the  $y$ -axis. The colors indicate the CP in the corresponding locations. It is observed that the CP is higher when the transmitter is closer to the wall, except in four corners of the room. A certain degree of location symmetry can also be observed in Fig. 8. Hence, it is concluded that the optimal location for a transmitter is near the wall except for the corners.

### C. CP variation with respect to $\lambda_s$ and $\lambda_o$

In this section, we investigate the CP performance variation over the RIS number and obstacle density. In Fig. 9, the CP performance is evaluated at four different Tx locations with respect to the RIS number at different room sizes when the obstacle density is fixed. Firstly, it is noted that the CP variation trend is similar (increase and then saturate) at different room sizes for all sub-figures. Secondly, it is noted that the CP performance has a significant increase in Fig. 9(a) and Fig. 9(c) (30% in Fig. 9(c) at  $a = 80$ ) with the increase of the total RIS number, while Fig. 9(b), and Fig. 9(d) do not show similar increase (maximum CP increase amount below 0.05). For Fig. 9(a) and Fig. 9(c), the trend of the curves can be explained by examining the variation of the expected values of  $D_{ts}$  with the increase of the total RIS number. With the increasing RIS number, the nearest RIS is approaching the projection point of the transmitter on the wall, which will lead to the decrease of the expected value of  $D_{ts}$ . This explains the CP increase in Fig. 9(a) and Fig. 9(c). Observing these two sub-figures carefully, we can also find that the increased amount of Fig. 9(c) is higher than Fig. 9(a) for every room size. This is because when optimizing the RIS location<sup>9</sup> in Fig. 9(a), the expected value of  $D_{sr}$  will increase, which will

<sup>9</sup>By saying optimizing the RIS location, we mean increasing the RIS number. Because the more RIS we have, the closer the nearest RIS to the projection point.

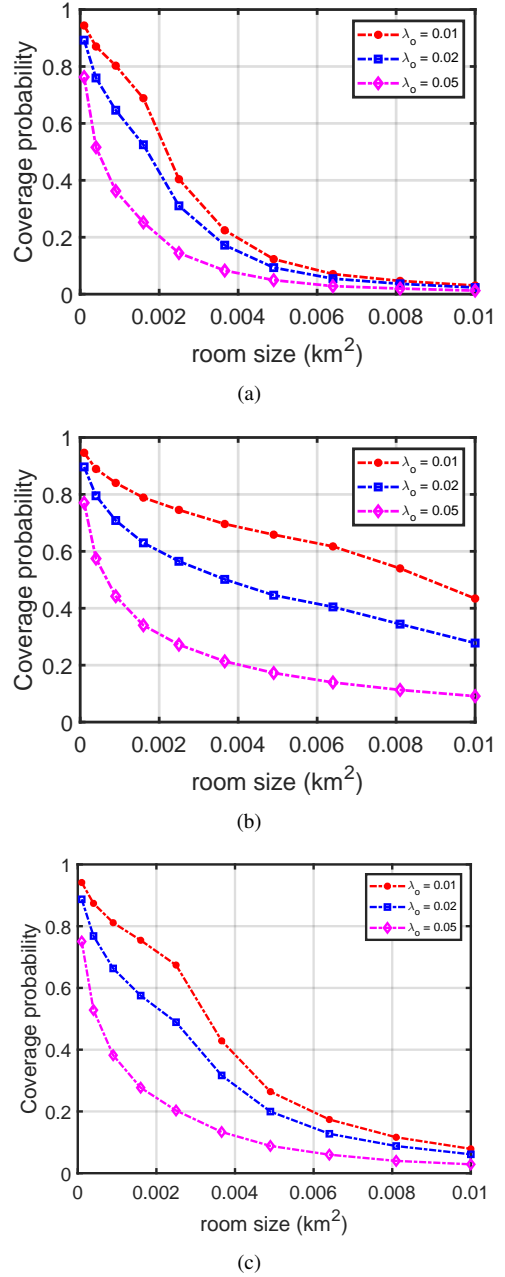


Fig. 7: (a) Performance of the RIS-assisted indoor network with the first transmitter location. (b) Performance of the RIS-assisted indoor network with the second transmitter location. (c) Performance of the RIS-assisted indoor network with the third transmitter location.

counteract the benefit brought by RIS location optimization. However, such phenomena do not exist when the transmitter is placed in the third location. For Fig. 9(b) and Fig. 9(d), it can be observed that the CP increased amount is not significant (below 0.05 for every room size) with the increase of the RIS number. This is due to the large expected value of  $D_{ts}$  even after the RIS location optimization. To investigate the improvement over CP made by the obstacle density and the RIS number, more simulation results are shown in Fig.10, where the CP performance variation is shown with respect to



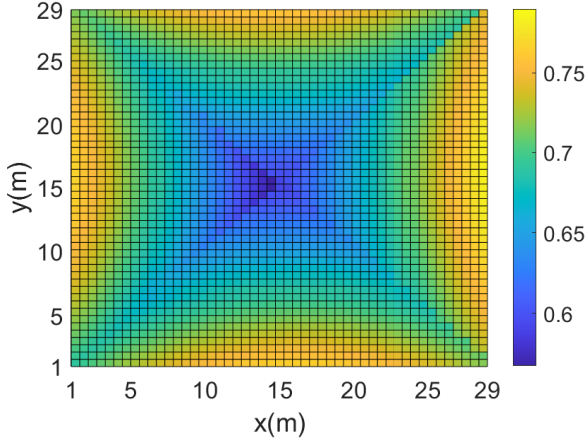


Fig. 8: Performance evaluation with respect to the transmitter's location in a 30-by-30 meters square room with RIS number on one wall  $n = 15$ ,  $0.02 \text{ points/m}^2$  obstacle density, and  $1 \times 10^{-3} \text{ W}$  transmitted power.

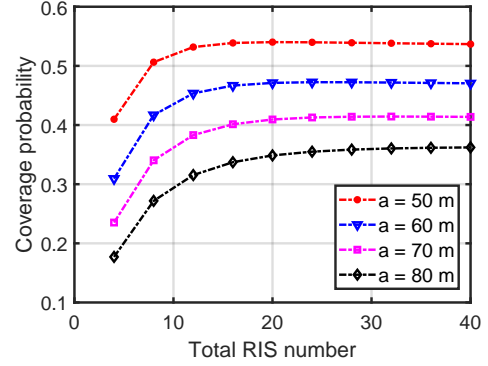
RIS number and obstacle density. Observing vertically, we can see that the CP performance will decrease with the increase in the obstacle density. However, the speed of decrease is smaller when the RIS number is high (e.g., 40) and bigger when the RIS number is low (e.g., 10). Observing horizontally, it is found that the obstacle density dominates the CP performance when the obstacle density exceeds  $0.05 \text{ points/m}^2$ . Below  $0.05 \text{ points/m}^2$ , the increase of the RIS number can improve the CP.

## V. CONCLUSION

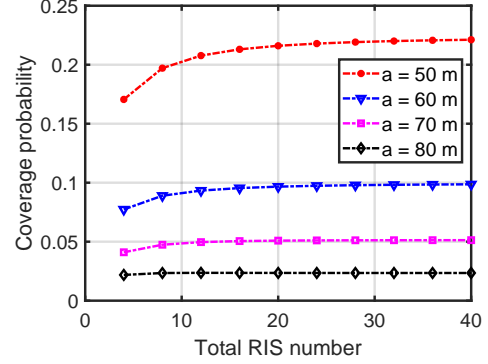
In this paper, we described an order statistic-based method for indoor THz wireless communication network performance analysis. We derived the analytical expression of the CP. Through comparison with the Monte Carlo simulation, it was verified that the analytical expression of the CP is accurate. We then showed the performance variation with respect to the room size, transmitter's location, obstacle density, and RIS number. The impact on the CP performance can be sorted as obstacle density, room size, total RIS number, and the transmitter's location. Although the effect of obstacles and room size is dominant to the CP, a significant CP improvement (around 15% of CP increase by optimizing the transmitter's location, and around 30% by increasing the RIS number) can also be observed with the transmitter location optimization and the increase of the total RIS number.

### APPENDIX A MORE $D_{ST}$ CDF COMPARISONS WITH DIFFERENT PARAMETERS

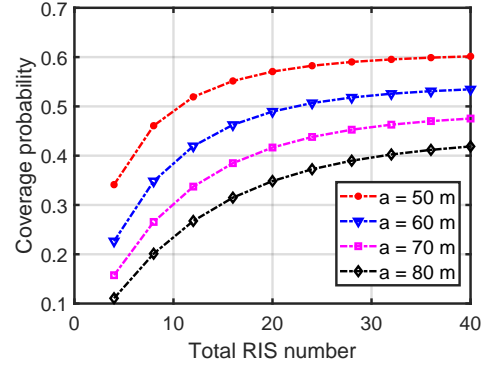
In Fig. 11(a), the transmitter is placed at the center of a square room that has a length of 30m. We can observe that the largest deviation happens when  $n = 1$ , which is around 0.05. In Fig. 11(b), the transmitter is placed at the center of a square room that has a length of 40m, similarly, the largest deviation happens when  $n = 1$ , and it is around 0.05. With



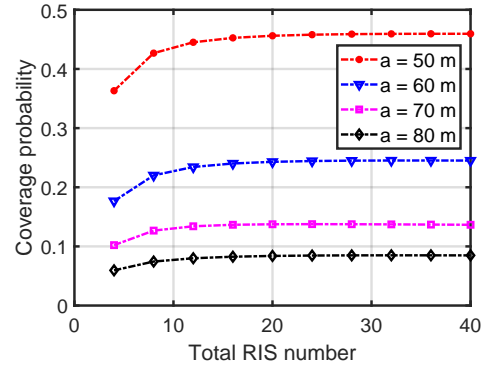
(a)



(b)



(c)



(d)

Fig. 9: (a)-(d) Performance evaluation with respect to the RIS number at different room sizes, with obstacle density being  $\lambda_o = 0.02 \text{ points/m}^2$ , transmitter location being the first, second, third, and fourth locations, and transmitted power being  $1 \times 10^{-3} \text{ W}$ .

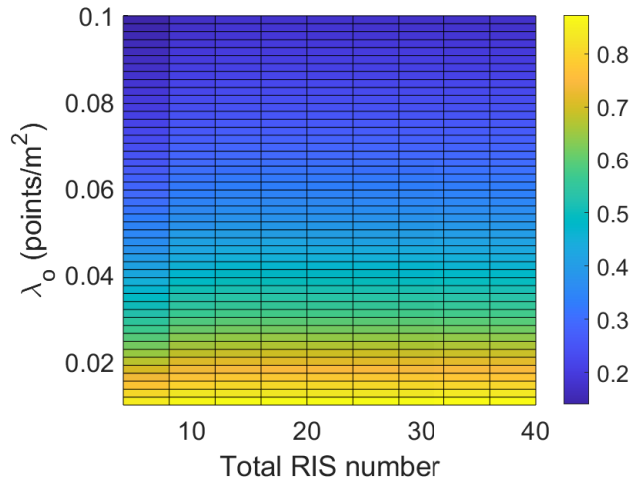


Fig. 10: Performance evaluation with respect to the RIS number and the obstacle density in a 30-by-30 meters square room with the transmitter located at the first location. The transmitted power is  $1 \times 10^{-3}$  W.

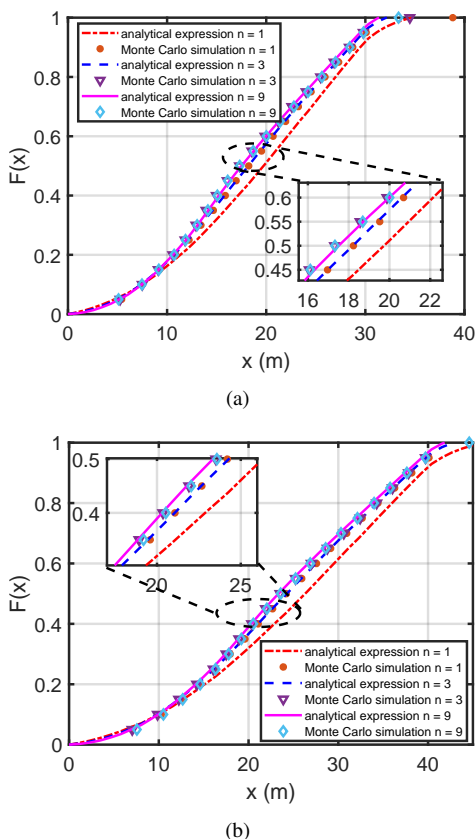


Fig. 11: (a) CDF of  $D_{sr}$  comparison between the Monte Carlo simulation and the analytical expression with  $a = 30$ ,  $x_t = 15\text{m}$ ,  $y_t = 15\text{m}$ , and the RIS number on a wall  $n = 1, 3, 9$ . (b) CDF of  $D_{sr}$  comparison between the Monte Carlo simulation and the analytical expression with  $a = 40$ ,  $x_t = 15\text{m}$ ,  $y_t = 15\text{m}$ , and the RIS number on a wall  $n = 1, 3, 9$ .

Fig. 4 and Fig. 11, we can assure that the approximation is accurate under different parameters.

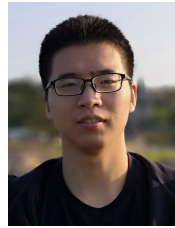
## REFERENCES

- [1] K. Danyluk, T. Ulusoy, W. Wei, and W. Willett, "Touch and beyond: Comparing physical and virtual reality visualizations," *IEEE Transactions on Visualization and Computer Graphics*, vol. 28, no. 4, pp. 1930–1940, 2020.
- [2] N. T. Banerjee, A. J. Baughman, S.-Y. Lin, Z. A. Witte, D. M. Klaus, and A. P. Anderson, "Side-by-side comparison of human perception and performance using augmented, hybrid, and virtual reality," *IEEE Transactions on Visualization and Computer Graphics*, vol. 28, no. 12, pp. 4787–4796, 2021.
- [3] S. Ghosh, L. Winston, N. Panchal, P. Kimura-Thollander, J. Hotnog, D. Cheong, G. Reyes, and G. D. Abowd, "Notifivr: Exploring interruptions and notifications in virtual reality," *IEEE transactions on visualization and computer graphics*, vol. 24, no. 4, pp. 1447–1456, 2018.
- [4] J. Guo, U. Kurup, and M. Shah, "Is it safe to drive? An overview of factors, metrics, and datasets for driveability assessment in autonomous driving," *IEEE Transactions on Intelligent Transportation Systems*, vol. 21, no. 8, pp. 3135–3151, 2019.
- [5] L. Claussmann, M. Revilloud, D. Gruyer, and S. Glaser, "A review of motion planning for highway autonomous driving," *IEEE Transactions on Intelligent Transportation Systems*, vol. 21, no. 5, pp. 1826–1848, 2019.
- [6] D. Feng, C. Haase-Schütz, L. Rosenbaum, H. Hertlein, C. Glaeser, F. Timm, W. Wiesbeck, and K. Dietmayer, "Deep multi-modal object detection and semantic segmentation for autonomous driving: Datasets, methods, and challenges," *IEEE Transactions on Intelligent Transportation Systems*, vol. 22, no. 3, pp. 1341–1360, 2020.
- [7] I. Union, "IMT traffic estimates for the years 2020 to 2030," *Report ITU*, vol. 2370, 2015.
- [8] K. B. Letaief, W. Chen, Y. Shi, J. Zhang, and Y.-J. A. Zhang, "The roadmap to 6G: AI empowered wireless network," *IEEE communications magazine*, vol. 57, no. 8, pp. 84–90, 2019.
- [9] K. Liu, S. Jia, S. Wang, X. Pang, W. Li, S. Zheng, H. Chi, X. Jin, X. Zhang, and X. Yu, "100 Gbit/s THz photonic wireless transmission in the 350-GHz band with extended reach," *IEEE Photonics Technology Letters*, vol. 30, no. 11, pp. 1064–1067, 2018.
- [10] H.-H. Lu, C.-Y. Li, W.-S. Tsai, R.-D. Lin, Y.-S. Tang, Y.-X. Chen, Y.-S. Lin, and W.-C. Fan, "An Integrated Fiber-FSO-5G NR Sub-THz Link With 86.112 Gbps High Aggregate Data Rates," *Journal of Lightwave Technology*, vol. 40, no. 24, pp. 7790–7798, 2022.
- [11] C. Chaccour, M. N. Soorki, W. Saad, M. Bennis, and P. Popovski, "Can terahertz provide high-rate reliable low-latency communications for wireless VR?," *IEEE Internet of Things Journal*, vol. 9, no. 12, pp. 9712–9729, 2022.
- [12] L. Fan, H. Wang, Q. Yang, Y. Wang, B. Deng, and H. Xiao, "High frame-rate and low-latency video SAR based on robust Doppler parameters estimation in the terahertz regime," *IEEE Transactions on Geoscience and Remote Sensing*, 2023.
- [13] Z. Chen, X. Ma, B. Zhang, Y. Zhang, Z. Niu, N. Kuang, W. Chen, L. Li, and S. Li, "A survey on terahertz communications," *China Communications*, vol. 16, no. 2, pp. 1–35, 2019.
- [14] M. Di Renzo, A. Zappone, M. Debbah, M.-S. Alouini, C. Yuen, J. De Rosny, and S. Tretyakov, "Smart radio environments empowered by reconfigurable intelligent surfaces: How it works, state of research, and the road ahead," *IEEE journal on selected areas in communications*, vol. 38, no. 11, pp. 2450–2525, 2020.
- [15] H.-J. Song, H. Hamada, and M. Yaita, "Prototype of KIOSK data downloading system at 300 GHz: Design, technical feasibility, and results," *IEEE Communications Magazine*, vol. 56, no. 6, pp. 130–136, 2018.
- [16] H. Zhao, L. Wei, M. Jarrahi, and G. J. Pottie, "Extending spatial and temporal characterization of indoor wireless channels from 350 to 650 GHz," *IEEE Transactions on Terahertz Science and Technology*, vol. 9, no. 3, pp. 243–252, 2019.
- [17] J. M. Eckhardt, T. Doeker, S. Rey, and T. Kürner, "Measurements in a real data centre at 300 GHz and recent results," in *2019 13th European Conference on Antennas and Propagation (EuCAP)*, pp. 1–5, IEEE, 2019.
- [18] A.-A. A. Boulgeorgos and A. Alexiou, "Outage probability analysis of THz relaying systems," in *2020 IEEE 31st Annual International Symposium on Personal, Indoor and Mobile Radio Communications*, pp. 1–7, IEEE, 2020.

- [19] S. Farrag, E. Maher, A. El-Mahdy, and F. Dressler, "Outage probability analysis of UAV assisted mobile communications in THz channel," in *2021 16th Annual Conference on Wireless On-demand Network Systems and Services Conference (WONS)*, pp. 1–8, IEEE, 2021.
- [20] Z. Lou, B. E. Y. Belmekki, and M.-S. Alouini, "Coverage analysis of hybrid RF/THz networks with best relay selection," *IEEE Communications Letters*, 2023.
- [21] J. Sayehvand and H. Tabassum, "Interference and coverage analysis in coexisting RF and dense terahertz wireless networks," *IEEE Wireless Communications Letters*, vol. 9, no. 10, pp. 1738–1742, 2020.
- [22] K. Humadi, I. Trigui, W.-P. Zhu, and W. Ajib, "Coverage analysis of user-centric dense terahertz networks," *IEEE Communications Letters*, vol. 25, no. 9, pp. 2864–2868, 2021.
- [23] A.-A. A. Boulogeorgos and A. Alexiou, "Error analysis of mixed THz-RF wireless systems," *IEEE Communications Letters*, vol. 24, no. 2, pp. 277–281, 2019.
- [24] P. Bhardwaj and S. M. Zafaruddin, "Performance of Dual-Hop Relaying for THz-RF Wireless Link Over Asymmetrical  $\alpha$ - $\mu$  Fading," *IEEE Transactions on Vehicular Technology*, vol. 70, no. 10, pp. 10031–10047, 2021.
- [25] P. Bhardwaj and S. M. Zafaruddin, "Fixed-gain AF relaying for RF-THz wireless system over  $\alpha$ - $\kappa$ - $\mu$  shadowed and  $\alpha$ - $\mu$  channels," *IEEE Communications Letters*, vol. 26, no. 5, pp. 999–1003, 2021.
- [26] S. Li and L. Yang, "Performance analysis of dual-hop THz transmission systems over  $\alpha$ - $\mu$  fading channels with pointing errors," *IEEE Internet of Things Journal*, vol. 9, no. 14, pp. 11772–11783, 2021.
- [27] G. Stratidakis, E. N. Papanotiropoulos, H. Konstantinis, A.-A. A. Boulogeorgos, and A. Alexiou, "Relay-based blockage and antenna misalignment mitigation in THz wireless communications," in *2020 2nd 6G Wireless Summit (6G SUMMIT)*, pp. 1–4, IEEE, 2020.
- [28] Y. Zhu, G. Zheng, and K.-K. Wong, "Stochastic geometry analysis of large intelligent surface-assisted millimeter wave networks," *IEEE Journal on Selected Areas in Communications*, vol. 38, no. 8, pp. 1749–1762, 2020.
- [29] T. Shafique, H. Tabassum, and E. Hossain, "Stochastic geometry analysis of IRS-assisted downlink cellular networks," *IEEE Transactions on Communications*, vol. 70, no. 2, pp. 1442–1456, 2022.
- [30] C. Zhang, W. Yi, Y. Liu, K. Yang, and Z. Ding, "Reconfigurable intelligent surfaces aided multi-cell NOMA networks: A stochastic geometry model," *IEEE Transactions on Communications*, vol. 70, no. 2, pp. 951–966, 2021.
- [31] M. A. Kishk and M.-S. Alouini, "Exploiting randomly located blockages for large-scale deployment of intelligent surfaces," *IEEE Journal on Selected Areas in Communications*, vol. 39, no. 4, pp. 1043–1056, 2020.
- [32] T. Bai, R. Vaze, and R. W. Heath, "Analysis of blockage effects on urban cellular networks," *IEEE Transactions on Wireless Communications*, vol. 13, no. 9, pp. 5070–5083, 2014.
- [33] T. Wang, G. Chen, M.-A. Badiu, and J. P. Coon, "Performance analysis of RIS-assisted large-scale wireless networks using stochastic geometry," *IEEE Transactions on Wireless Communications*, 2023.
- [34] H. T. P. Da Silva, M. S. De Alencar, W. J. L. Queiroz, and H. S. Silva, "Coverage Probability Analysis of a RIS-Assisted THz Indoor System Based on Ray Tracing Simulations," in *2023 IEEE Latin-American Conference on Communications (LATINCOM)*, pp. 1–6, IEEE, 2023.
- [35] O. Abbas, N. Kouzayha, M. Kishk, H. Sarraddeden, M.-S. Alouini, and T. Y. Al-Naffouri, "Performance Analysis of Indoor THz Networks with Intelligent Reflective Surfaces," in *ICC 2023-IEEE International Conference on Communications*, pp. 2816–2821, IEEE, 2023.
- [36] Z. Li, H. Hu, J. Zhang, and J. Zhang, "Enhancing indoor mmWave wireless coverage: Small-cell densification or reconfigurable intelligent surfaces deployment?," *IEEE Wireless Communications Letters*, vol. 10, no. 11, pp. 2547–2551, 2021.
- [37] H. Qin, Z. Liu, and C. Yang, "Indoor mm-wave coverage enhancement: Reconfigurable intelligent surface deployment strategy based on human mobility model," *IEEE Communications Letters*, vol. 26, no. 10, pp. 2475–2479, 2022.
- [38] A. M. Mathai, *An introduction to geometrical probability: distributional aspects with applications*, vol. 1. CRC Press, 1999.
- [39] Ö. Özdoğan, E. Björnson, and E. G. Larsson, "Intelligent reflecting surfaces: Physics, propagation, and pathloss modeling," *IEEE Wireless Communications Letters*, vol. 9, no. 5, pp. 581–585, 2019.
- [40] W. Tang, M. Z. Chen, X. Chen, J. Y. Dai, Y. Han, M. Di Renzo, Y. Zeng, S. Jin, Q. Cheng, and T. J. Cui, "Wireless communications with reconfigurable intelligent surface: Path loss modeling and experimental measurement," *IEEE Transactions on Wireless Communications*, vol. 20, no. 1, pp. 421–439, 2020.



**Zhi Chai** received his B.Sc. and M.Sc from Xidian University and University College London in 2020 and 2021. He is a Ph.D. student in the Engineering Science Department at the University of Oxford. His current research interests include liquid crystal-based reconfigurable intelligent surface modeling, stochastic geometry-based reconfigurable intelligent surface-assisted network performance analysis, and terahertz communications.



**Jiajie Xu** [S'19, M'24] received his M.Sc. and Ph.D. degrees from Yanshan University and King Abdullah University of Science and Technology (KAUST) in 2019 and 2023. He is a postdoctoral research fellow in the communication theory lab at KAUST. His current research interests include underwater wireless acoustic communication, underwater target detection, underwater cooperative networks, maritime communication, space-air-ground-sea integrated communication systems and joint sensing and communication systems, stochastic geometry, and energy harvesting wireless networks.



**Mohamed-Slim Alouini** [S'94-M'98-SM'03-F'09] was born in Tunis, Tunisia. He received the Ph.D. degree in Electrical Engineering from the California Institute of Technology (Caltech) in 1998. He served as a faculty member at the University of Minnesota then in the Texas A&M University at Qatar before joining in 2009 the King Abdullah University of Science and Technology (KAUST) where he is now a Distinguished Professor of Electrical and Computer Engineering. Prof. Alouini is a Fellow of the IEEE and of the OSA. He is currently particularly

interested in addressing the technical challenges associated with the uneven distribution, access to, and use of information and communication technologies in far-flung, rural, low-density populations, low-income, and/or hard-to-reach areas.



**Justin P. Coon** Justin P. Coon received a BSc degree (with distinction) in electrical engineering from the Calhoun Honours College, Clemson University, USA and a PhD in communications from the University of Bristol, UK in 2000 and 2005, respectively. He held various research positions at Toshiba Research Europe Ltd. (TREL) from 2004 until 2013, including the position of Research Manager from 2010 to 2013, during which time he led all research on physical layer communications and network science at TREL. Dr. Coon was a Visiting

Fellow with the School of Mathematics at the University of Bristol, UK from 2010 until 2012, and he held a position as Reader in the Department of Electrical and Electronic Engineering at the same university from 2012 to 2013. He joined the University of Oxford in 2013 where he is currently a Professor of Engineering Science as well as the Emmott Fellow in Engineering Science at Oriel College. Dr. Coon is the recipient of Toshiba's Distinguished Research Award for his work on 4G systems and has received three "best paper" awards. He has published more than 200 papers in IEEE and APS journals and conferences and is a named inventor on more than 30 patents. He has served as an Editor for several IEEE journals and has chaired or co-chaired various IEEE conferences.